Retrieval of Cloud Condensation Nuclei Number Concentration Profiles from Lidar Extinction and Backscatter Data

Min Lv[1], Zhien Wang[2], Zhanqing Li[1,3]*, Tao Luo[4], Richard Ferrare[5], Dong Liu[4], Decheng Wu[4], Jietai Mao[6], Bingcheng Wan[7], Fang Zhang[1], Yuying Wang[1]

[1]State Key Laboratory of Earth Surface Processes and Resource Ecology and College of Global Change and Earth System Science, Beijing Normal University, Beijing, China,

[2] Department of Atmospheric Science, University of Wyoming, Laramie, Wyoming, USA,

[3]University of Maryland, College Park, Maryland, USA,

[4]Key Laboratory of Atmospheric Composition and Optical Radiation, Anhui Institute of Optics and Fine Mechanics, Chinese Academy of Sciences, Anhui, China,

[5] NASA Langley Research Center, Hampton, Virginia, USA

[6]School of Physics, Peking University, Beijing, China,

[7]State Key Laboratory of Atmospheric Boundary Layer Physics and Atmospheric Chemistry, Institute of Atmospheric Physics, Chinese Academy of Sciences, Beijing, China.

Corresponding author: Zhanqing Li, zhanqing@umd.edu

Key Points:

- An algorithm is proposed to retrieve vertical profiles of CCN from lidar measurements
- The potential of the algorithm is demonstrated with numerical simulations and observations
- CCN retrievals from lidar are in good agreement with in situ measurements

Abstract

25
26   The vertical distribution of aerosols and their capability of serving as cloud condensation nuclei

27   (CCN) are important for improving our understanding of aerosol indirect effects. Although

28   ground-based and airborne CCN measurements have been made, they are generally scarce,

29   especially at cloud base where it is needed most. We have developed an algorithm for profiling

30   CCN number concentrations using backscatter coefficients at 355, 532, and 1064 nm and

31   extinction coefficients at 355 and 532 nm from multi-wavelength lidar systems. The algorithm

32   considers three distinct types of aerosols (urban industrial, biomass burning, and dust) with

33   bimodal size distributions. The algorithm uses look-up tables, which were developed based on the

34   ranges of aerosol size distributions obtained from the Aerosol Robotic Network, to efficiently find

35   optimal solutions. CCN number concentrations at five supersaturations (0.07–0.80%) are

36   determined from the retrieved particle size distributions. Retrieval simulations were performed

37   with different combinations of systematic and random errors in lidar-derived extinction and

38   backscatter coefficients: systematic errors range from -20% to 20% and random errors are up to

39   15%, which fall within the typical error ranges for most current lidar systems. The potential of this

40   algorithm to retrieve CCN concentrations is further evaluated through comparisons with surface-

41   based CCN measurements with near surface lidar retrievals. This retrieval algorithm would be

42   valuable for aerosol-cloud interaction studies for which virtually none has employed CCN at cloud

43   base because of the lack of such measurements.

1. Introduction

Atmospheric aerosol particles affect climate indirectly by acting as cloud condensation nuclei (CCN) [*Carslaw et al.*, 2010; *Paasonen et al.*, 2013]. CCN are those aerosol particles on which cloud droplets form when the supersaturation in a cloud is high enough for the particles to grow by water condensation until they reach a critical radius, beyond which condensational growth continues spontaneously unless the supersaturation decreases rapidly [*Nenes et al.* 2001b; *Mamouri and Ansmann*, 2016]. Anthropogenic emissions of aerosol particles are a major source of CCN, which influence cloud microphysical and radiative properties, and consequently climate change [*Boucher et al.*, 2013]. Therefore, an accurate knowledge of the spatial distribution of aerosols and their capability of serving as CCN is fundamental to understanding aerosol indirect effects. As emphasized by *Fan et al.* [2016], obtaining concurrent measurements of aerosol properties and cloud microphysical and dynamic properties over a range of temporal and spatial scales is critical to advance our understanding of aerosol-cloud interactions.

CCN can be measured in situ from the ground [*Feingold and Grund*, 1994; *Roberts and Nenes*, 2005] and from aircraft [*Rosenfeld et al.*, 2008; *Li et al.*, 2015a, b], or inferred from satellite observations [*Grandey and Stier*, 2010; *Gryspeerdt et al.*, 2014; *Shinozuka et al.*, 2015; *Rosenfeld et al.*, 2016]. Long-term monitoring of CCN properties at different observation sites has been chiefly made on the ground. Other than limited horizontal cover and many other issues [*Paramonov et al.*, 2013], near-surface CCN properties could be significantly different from CCN properties near the cloud base due to vertical aerosol inhomogeneities, especially air pollution under stable atmospheric boundary conditions. Except for *Rosenfeld et al.* [2016], satellite-based CCN estimations mainly use aerosol optical depth as a proxy for aerosol loading to take advantage of its global coverage. It is still challenging and highly uncertain [*Andreae*, 2009; *Liu and Li*, 2014] with many other limitations such as a lower temporal resolution, cloud contamination, and aerosol swelling in the moist environment near clouds [*Koren et al.*, 2007]. Airborne measurements can provide CCN measurements near cloud base, but are expensive to collect and are limited to a few field experiments [*Feingold et al.*, 1998; *Li et al.*, 2015a, b]. The capability of routinely measuring new CCN at cloud base to study aerosol-cloud-precipitation interactions effectively is still lacking [*Burkart et al.*, 2011].

73   Vertically-resolved aerosol measurements offered by lidars provide the potential to measure

74   CCN near cloud base. *Feingold et al.* [1998] developed an approach that used a combination of

75   several remote sensing instruments, such as the Ka-band Doppler radar, the microwave radiometer,

76   and the lidar, to derive the activation of CCN as a function of supersaturation level. However, this

77   approach is based on the Junge power-law aerosol size distribution [*Junge*, 1952] that is only

78   applicable for a clean troposphere and stratosphere. *Ghan and Collins* [2004] and *Ghan et al.* [2006]

79   developed a technique to estimate CCN at cloud base based on the relationship between the aerosol

80   extinction from lidar and CCN concentrations from near-surface measurements. However, their

81   methods rely on the assumption that the aerosol composition and the shape of the aerosol size

82   distribution at the surface are representative of the vertical column. Thus, their retrievals may have

83   high uncertainties if the vertical profile of the shape of the aerosol size distribution differs

84   markedly from that at the surface. In addition to their common use in profiling atmospheric

85   temperature and humidity [*Wandinger*, 2005], multi-wavelength Raman lidars and High Spectral

86   Resolution Lidars (HSRL) have been increasingly used in recent years to retrieve aerosol and CCN

87   properties [*Müller et al.*, 1999; *Chemyakin et al.*, 2014; *Mamouri and Ansmann*, 2016]. This type

88   of lidar allows for independent inferences of particle backscatter and extinction coefficients

89   without the need for assuming any atmospheric parameters. Multi-wavelength Raman lidars can

90   thus be used to quantify the main aerosol microphysical parameters and CCN properties with fewer

91   a priori assumptions. The retrieval of aerosol microphysical properties is mainly based on the

92   regularization algorithm [*Müller et al.*, 1999, 2000, 2014; *Veselovskii et al.*, 2002, 2004, 2013;

93   *Chemyakin et al.*, 2014, 2016]. Most of these early studies focused on aerosol size distribution and

94   total aerosol concentration retrievals, and used the regularization technique, which lead to higher

95   sensitivities with a 1-sigma value of 61.4–95.2% for different aerosol types [*Pérez-Ramírez et al.*,

96   2013]. This is because total aerosol concentration is very sensitive to aerosols with diameters

97   smaller than 50 nm and lidar observations offer almost no constraint for them. To ourknowledge,

98   limited attempts have been made to quantify CCN concentrations from multi-wavelength lidar

99   measurements. *Feingold and Grund* [1994] explored the potential of using multi-wavelength lidar

100   measurements, but they only performed a simulation by using the theoretical wavelengths of289,

101   532,1064, 2020 and 11150 nm that some wavelengths are not available in real measurements.

102   From the simulation, they only provided some relationships between multi-wavelength backscatter

103   coefficients with the median radius and did not quantify any aerosol or CCN parameter.

104 In this paper, we propose a retrieval approach to estimate CCN number concentrations from

105 multi-wavelength lidar extinction and backscatter coefficients. The approach is implemented with

106 look-up tables (LUTs) to provide stable and efficient retrievals. CCN number concentrations at

107 five critical supersaturation ratios (S_cs, 0.07–0.80%) are determined from the retrieved aerosol size

108 distributions. The retrieval accuracies are evaluated using simulated lidar extinction and

109 backscatter coefficients with both random and systematic errors. Since CCN retrievals are less

110 sensitive to uncertainties in very small particles (nucleation-mode particles), it leads to much

111 smaller errors in the retrievals of CCN number concentration than those focusing on total aerosol

112 number concentrations as was done by most early studies due to little information on fine-mode

113 aerosols from available lidar measurements. In Section 2, the inversion methodology is described.

114 In Section 3, we present the numerical simulations. In Section 4, a real case study is presented.

115 Conclusions are given in Section 5.

116 **2. Methodology**

117 **2.1 Aerosol size distributions**

118 As demonstrated by *Baars et al.* [2016], aerosol types can be identified by combining their

119 Ångstrom exponent, lidar ratio, and depolarization ratio from multi-wavelength HSRL or Raman-

120 polarization lidar measurements [*Burton et al.*, 2012; *Groß et al.*, 2013]. Therefore, our study

121 assumes known aerosol types for CCN retrievals for the sake of tackling other more challenging

122 tasks in retrieving CCN profiles.

123 Initially, three common and distinct aerosol types are considered in this study: urban industrial

124 aerosols (Type 1), biomass-burning aerosols (Type 2), and dust aerosols (Type 3). Although

125 particle size distributions are not always bimodal in each measurement case, their size distributions

126 can be treated as a combination of fine and coarse modes with lognormal distributions, as widely

127 used in aerosol remote sensing studies [*Veselovskii et al.*, 2004; *Remer et al.*, 2005; *Schuster et al.*,

128 2006]. Multi-wavelength HSRL or Raman lidar measurements provide feasible constraints on

129 these size parameters:

130
$$\frac{dn(r)}{d\ln(r)} = \sum_{i=f,c} \frac{N_{ti}}{(2\pi)^{1/2}\ln\sigma_i} \exp\left[-\frac{\left(\ln r - \ln r_i^n\right)^2}{2\left(\ln\sigma_i\right)^2}\right], \tag{1}$$

131 where N_{ti} is the total particle number concentration of the ith mode and r_i^n is the median radius for

132 the aerosol size distribution with n representing the number concentration distribution. The index

133   $i = f, c$ refers to the fine mode and coarse mode, respectively. The term $\ln\sigma_i$ is the mode width of

134   the ith mode. This general aerosol size distribution shape is adopted in this study to improve the

135   accuracy of the CCN retrieval. The sensitivity test regarding the response of CCN to the

136   assumption of bimodal size distributions is presented in Section 3.2.

137   Table 1 lists the typical ranges of the bimodal distribution parameters of the three types of

138   aerosols derived using measurements from sun and sky-scanning ground-based automated

139   radiometers at 12 selected Aerosol Robotic Network (AERONET) sites from 1993 to 2000

140   [*Dubovik et al.*, 2002; *Veselovskii et al.*, 2004]. Parameters representing the volume concentration

141   can be transformed to parameters for the number concentration through the following relationships

142   [*Horvath et al.*, 1990]:

$$r_i^n = r_i^v / \exp\left[3\left(\ln\sigma\right)^2 \right], \tag{2}$$

$$V_{ti} = N_{ti} \frac{4}{3}\pi\left(r_i^n\right)^3 \exp\left[\frac{9}{2}\left(\ln\sigma\right)^2 \right]. \tag{3}$$

145   As shown in Table 1 and Fig. 1, the main difference between the three aerosol types is the ratio

146   of the volume concentration of the fine mode to the volume concentration of the coarse mode.

147   Both urban industrial and biomass-burning aerosols have a predominance of fine-mode fractions

148   while the coarse mode dominates for dust aerosols.

2.2 Inversion technique for aerosol size distribution parameters

150   The first step in estimating CCN concentrations is to retrieve aerosol size distributions from

151   backscatter coefficients at 355, 532, and 1064 nm ($\beta_{355}, \beta_{532}, \beta_{1064}$) and extinction coefficients at

152   355 and 532 nm ($\alpha_{355}, \alpha_{532}$). These can be retrieved from multi-wavelength Raman lidar [*Ansmann*

153   *et al.*, 1992] or HSRL measurements [*Shipley et al.*, 1983]. Aerosol type, which can be identified

154   from lidar measurements [*Burton et al.*, 2012; *Groß et al.*, 2013; *Baars et al.* 2016] provides the

155   mean complex refractive index (Table 1). Thus, retrieving six parameters ($\sigma_f, N_{tf}, r_f, \sigma_c, N_{tc}, r_c$) for

156   a bimodal size distribution from five known quantities ($\beta_{355}, \beta_{532}, \beta_{1064}, \alpha_{355}, \alpha_{532}$) is still an ill-

157   defined problem. Observations [*Dubovik et al.*, 2002] indicate that the variation of the mode width

158   of the coarse mode ($ln\sigma_c$) is small for a given aerosol type and that the contribution of the coarse

159   mode to the total aerosol number concentration is relatively low. Therefore, we assume that $ln\sigma_c$

160   is a known quantity (Table 1). The retrieval errors from this assumption are examined in Section

161   3.3.

162   The retrieval algorithm searches for the best combination of five values (σ_f, N_{tf}, r_f, N_{tc}, r_c) to

163   match inputs (β_{355}, β_{532}, β_{1064}, α_{355}, α_{532}) by minimizing the following function:

$$\rho^{sum} = \sum_i \left| \frac{g_i - g_i^{'}}{g_i} \right|, \ (i = 1,...,5), \tag{4}$$

164

165   where g_i represents input optical data (β_{355}, β_{532}, β_{1064}, α_{355}, α_{532}), and $g_i^{'}$ is optical data ($\beta^{'}_{355}$,

166    $\beta^{'}_{532}$, $\beta^{'}_{1064}$, $\alpha^{'}_{355}$, $\alpha^{'}_{532}$) calculated from Mie theory and size distribution parameters. Note that

167   using the Mie theory for irregular-shaped dust aerosols can introduce potential systematic errors.

168   It is a simplification for this simulation study. For future real-case applications, an improved

169   optical database for dust aerosols will be developed following more advanced scattering

170   calculations [*Nousiainen*, 2009; *Liu et al.*, 2015]. Additionally, including depolarization

171   measurements improves not only the ability to distinguish dust, but also overall dust retrievals

172   [*Luo et al.*, 2015].

173   To search for the optimal solution, look-up tables (LUTs) for each type of aerosol are

174   constructed. To reduce the LUT size and its dimensions, each LUT consists of two parts. The size

175   distribution shown in Eq. (1) can be rewritten as

$$\overline{\frac{dn(r)}{dln(r)}} = \sum_{i=f,c} \left\{ \frac{1}{(2\pi)^{1/2} \ln\sigma_i} \exp\left[-\frac{\left(\ln r - \ln r_i^n\right)^2}{2\left(\ln\sigma_i\right)^2} \right] \bullet N_{ti} \right\} = \sum_{i=f,c} B_i \bullet N_{ti}, \tag{5}$$

176

177   where B_f and B_c refer to the data bank pre-computed with (σ_f, r_f, r) and (σ_c, r_c, r), respectively,

178   where the intervals of σ_f, r_f, and r_c are fixed at 0.01, 0.002, and 0.01 μm, respectively, and where

179   σ_c is assumed known and taken from Table 1. The range of r in the calculations is limited to 0.01–

180   10 μm with a fixed bin size of 0.002 defined on a logarithmic-equidistant scale. These intervals

181   are set as a compromise between accuracy and computation time.

182   Since the range of N_{tf} is usually large, the successive approximation method [*Kantorovitch*,

183   1939] is adopted:

184 Step 1: Calculate the corresponding optical data (β'_{355}, β'_{532}, β'_{1064}, α'_{355}, α'_{532}) from the data bank

185 (B_f, B_c) and N_{tf}, N_{tc} (the step widths of N_{tf} and N_{tc}: 100 and 0.1 cm^{-3}, respectively). Search for an

186 approximate solution based on the criterion in Eq. (4).

187 Step 2: Determine a smaller solution space of N_{tf} based on the approximate solution obtained in

188 Step 1. Repeat the procedure in Step 1 except use a smaller step width of 10 cm^{-3} for N_{tf}. Search

189 for the optimal solution of five parameters (σ_f, N_{tf}, r_f, N_{tc}, r_c).

190 **2.3 CCN estimations**

191   The ability of aerosols to act as CCN is mainly determined by three factors: aerosol particle

192 size distribution, chemical composition, and mixing state. Several studies have suggested that it is

193 controlled more by the aerosol size distribution than the chemical composition [*Junge and*

194 *McLaren*, 1971; *Fitzgerald,* 1973; *Dusek et al.*, 2006], however, for some specific areas and

195 meteorological conditions, both factors are important [*Mamouri and Ansmann*, 2016]. If no

196 suitable chemical composition data are available, using mean chemical composition information

197 for each aerosol type denoted by a single value of κ is feasible to estimate the CCN number

198 concentration. In reality, the uncertainty of using the mean value of κ to estimate the CCN number

199 concentration varies with atmospheric conditions. Most studies show that the uncertainty is within

200 10% [*Jurányi et al.*, 2010; *Deng et al.*, 2011; *Wang et al.*, 2018]. The hygroscopicity parameter κ

201 describes the relationship between the particle dry diameter and CCN activity when compositional

202 data are not available [*Petters and Kreidenweis*, 2007]. *Wang et al.*, [2018] found that the

203 sensitivity of the estimated CCN concentration to κ depends strongly on the variability of the shape

204 of the aerosol size distribution. The sensitivity of CCN concentration to κ becomes weaker with

205 increasing supersaturations, suggesting that chemical composition becomes less important in CCN

206 concentration estimates at larger supersaturations. In addition, this study also suggested that using

207 the mean value of $\kappa \approx 0.3$ can be a good proxy for urban industrial aerosol when estimating the

208 CCN concentration. The κ is assumed to be 0.3 for Type 1 [*Liu et al.*, 2011], 0.1 for Type 2 [*Petters*

209 *et al.*, 2009], and 0.03 for Type 3 [*Koehler et al.*, 2009] aerosols in the simulations. For actual

210 measurements, the mixing state of aerosols and the precise values of κ can be determined with the

211 aid of other instruments, such as the aerosol particle mass analyzer (APM), and the hygroscopic

212 tandem differential mobility analyzer (HTDMA) [*Malloy et al.*, 2009; *Zhang et al.*, 2014; *Wang et*

213 *al.*, 2017]. For experiments without the HTDMA, a lidar can be used to roughly infer κ indirectly

214   by identifying aerosol types [*Baars et al.*, 2016]. However, the determination of κ is beyond the

215   scope of the current method.

216   We first determine the critical radius (r_c) of CCN activation at five critical S_cs for activation

217   (0.07, 0.10, 0.20, 0.40, and 0.80%), which are often used for in CCN counters. The critical diameter

218   D_c ($r_c = D_c / 2$) and S_c for activation (where $S_c = S - 1$) can be computed from the maximum of κ-

219   Köhler curve as suggested by *Petters and Kreidenweis* [2007]:

220
$$S(D)=\frac{D^3 - D_d^3}{D^3 - D_d^3(1-\kappa)}\exp\left(\frac{4\sigma_{s/a}M_w}{RT\rho_w D}\right),\tag{6}$$

221   where S is the water saturation ratio, D is the droplet diameter, D_d is the dry diameter, $\sigma_{s/a} = 0.072$

222   J m^{-2}, M_w is the molecular weight of water, R is the universal gas constant, T is temperature and

223   equal to 298.15 K, and ρ_w is the density of water. Equation (6) describes the relationship between

224   the dry diameter and critical supersaturation for a selected hygroscopicity κ. Note that the Köhler

225   theory used for dust CCN activation is based on the assumptions that activation is solely controlled

226   by the amount of soluble salts in the dust aerosol and that it is not affected by water adsorption on

227   the dust surface.

228   Figure 2 shows the relationship between critical dry diameter and critical supersaturation for

229   each type of aerosol. Table 2 shows the critical radius (r_c) at five critical S_cs calculated using Eq.

230   (6). The critical radius for each type of aerosol in Table 2 shows that CCN retrievals are mostly

231   sensitive to particles with radii greater than 0.1 μm under normal atmospheric conditions, which

232   indicates that neglecting nucleation-mode particles has a weaker impact on CCN determination

233   than on the total aerosol number concentration retrievals.

234   It is noted that, to simplify the simulation, the impact of aerosol hygroscopic growth on the size

235   distributions is not considered. However, in real atmosphere, the aerosol size distribution is

236   affected by aerosol hygroscopic properties, especially when it is under high relative humidity

237   conditions or near cloud base. In this case, the wet size distribution should be corrected to the dry

238   size distribution by using the hygroscopic enhancement factor that is defined as

239
$$f(RH,r)=\frac{\xi(RH,r)}{\xi(RH_{ref},r)}\tag{6}$$

240   where *RH* is the relative humidity, *r* is the dry radius, $\xi(RH, r)$ refers to a *RH*-dependent aerosol

241   property at a certain *r*, the RH_{ref} is chosen as the lowest value of *RH* that represents the relative

242   dry environment in a case. $f(RH, r)$ can be obtained from HTDMA or Raman lidar [*Veselovskii*

243   *et al.*, 2009; *Lv et al.* 2017]. For the determination of *f(RH)* from Raman lidar, it is based on the

244   assumption of well-mixed atmospheric conditions that may be identified as having the constant

245   profiles of potential temperature and water vapor simultaneously [*Granados-Muñoz et al.*, 2015].

246   Finally, the CCN concentration can be calculated as

$$N_{ccn} = \int_{\ln r_c}^{\infty} \frac{dn(r)}{d \ln(r)} d\ln(r) \ . \tag{7}$$

3. Numerical simulations

249   Due to the lack of reliable collocated CCN and lidar measurements, evaluating the algorithm

250   is a challenging task. As the first step, the performance of the algorithm is evaluated using

251   simulated observations with different error characteristics.

3.1 Inversion with error-free inputs

253   The first evaluation is performed under the assumption of error-free lidar measurements to

254   understand the inversion stability. For each type of aerosol, 1000 different sets of bimodal size

255   distributions are used to simulate lidar observations. The retrieval is repeated for each simulated

256   observation. The retrieved parameters (σ_f, N_{tf}, r_f, N_{tc}, r_c) and assumed σ_c permit us to calculate the

257   errors in retrieved CCN number concentration (CCN$_{retrieved}$) with respect to the initial inputs

258   (CCN$_{initial}$), i.e., [(CCN$_{retrieved}$ - CCN$_{initial}$)/ CCN$_{initial}$] * 100%. Apart from the mean values, we

259   employ the standard deviations (SDs) of the CCN retrieval errors from the different bimodal size

260   distribution datasets to gauge the range of the retrieved CCN errors as well. As shown in Table 3,

261   initial CCN concentrations are well reproduced from the error-free inputs for each type of aerosol

262   size distribution. The mean errors in retrieved CCN number concentrations are close to zero, but

263   are not equal to zero due to striking an appropriate balance between the accuracy and processing

264   time of the LUTs as mentioned in section 2.2. The higher the accuracy of the LUTs, the more time

265   expensive are the calculations and the closer CCN errors approach zero. Moreover, the small SDs

266   ($\lesssim$ ~0.3%) suggest that the variances of errors among the different aerosol size distributions are

267　also small. Overall, the retrieval results shown in Table 3 attest to the good accuracy and stability

268　of the inversion algorithm for the three types of aerosols.

269　**3.2 Sensitivity test of the assumed bimodal size distribution with error-free inputs**

270　　　We test the sensitivity of the CCN retrieval to the assumption of the bimodal size distribution

271　by exploring dust aerosol size distributions measured on 20 August 2006 during the NASA African

272　Monsoon Multidisciplinary Analysis (NAMMA) campaign [Chen et al., 2011]. NAMMA particle

273　size distributions were measured simultaneously by an Ultra-High Sensitivity Aerosol

274　Spectrometer (UHSAS) for the 0.07–1 μm (geometric) diameter range [*Cai et al*., 2008] and a TSI

275　model 3321 Aerodynamic Particle Sizer (APS) for the 0.7–5 μm (aerodynamic) diameter range

276　[*Peters and Leith*, 2003]. Fifty full particle size distributions were constructed using the size

277　conversion factor, which is defined as the ratio of aerodynamic diameter to geometric diameter.

278　These full aerosol size distributions can be well represented by the tri-modal lognormal

279　distributions reported by Chen et al. [2011]. For the purpose of this study, we produce

280　corresponding bimodal fits representative of the observed size distributions. Figure 3 shows an

281　example of the observed aerosol size distribution and the corresponding bimodal fits. It suggests

282　that the observed dust aerosol size distributions can be qualitatively well represented by bimodal

283　lognormal size distributions. To quantify the errors arising from the bimodal lognormal fits, we

284　calculate CCN concentrations based on the bimodal-fits and compare them with those from the 50

285　observed size distributions. The κ of NAMMA dust aerosols is assumed to be 0.03 when

286　calculating CCN concentrations at the five values of S_cs as described in Section 2.3. Table 4 shows

287　the induced CCN errors from the bimodal fitting of 50 NAMMA aerosol size distributions. The

288　absolute value of CCN retrieval errors is 4.2% with a SD of 3.3% when S_c = 0.20%. Although

289　errors from the bimodal assumption are not negligible, the results suggest that bimodal lognormal

290　aerosol size distributions are adequate for retrieving CCN concentrations.

291　**3.3 Sensitivity test of the assumed lnσ_c with error-free inputs**

292　　　As described in section 2.2, lnσ_c is assumed to be equal to 0.7, 0.7, and 0.65 in LUTs

293　corresponding to the different aerosol types. However, the real lnσ_c may vary within a small range.

294　A sensitivity test of the effects of this assumption on the retrieval results is performed. In this

295　sensitivity test, the fixed values of lnσ_c are still used in the LUTs while the real values of lnσ_c in

296　simulations is selected randomly from within the ranges 0.6–0.8, 0.7–0.8, and 0.6–0.7 for urban

297   industrial, biomass-burning, and desert dust aerosols, respectively [*Veselovskii et al.*, 2004]. One

298   thousand different sets of simulations are produced randomly with the other known parameters as

299   input. The same inversion procedure described in Section 3.1 is repeated to retrieve CCN

300   concentrations and to calculate the retrieval errors.

301   Table 5 shows CCN retrieval errors due to assuming a constant $\ln\sigma_c$. As expected, the

302   assumption of a constant $\ln\sigma_c$ introduces an additional CCN retrieval error. In general, CCN

303   retrieval errors at higher S_cs are larger than those at lower S_cs for all types of aerosols due to the

304   smaller critical radius, which makes CCN calculations more sensitive to fine-mode size

305   distribution shapes. The maximum absolute value of CCN errors is 3.4% when S_cs are 0.07% and

306   0.10%, and reaches 6.6% when the S_c is 0.80%. This suggests that assuming a constant $\ln\sigma_c$ is

307   reasonable although the errors resulting from the assumption are not negligible.

3.4 Effect of systematic and random errors on the retrieval results

3.4.1 The impact of systematic errors

310   Extinction and backscatter coefficients retrieved from multi-wavelength lidar measurements

311   contain systematic and random errors [*Ansmann et al.*, 1992]. Systematic errors can be induced by

312   experiment conditions, techniques, and our understanding of physical interactions. Systematic

313   errors ranging from -20% to 20% in intervals of 5% are considered for the extinction and

314   backscatter coefficients. In actual measurements, the Raman lidar or HSRL allows for the

315   independent calculation of extinction and backscatter coefficients by combining elastic and Raman

316   backscatter signals [*Ansmann et al.*, 1992] and by taking advantage of the spectral distribution of

317   the lidar return signal to discriminate aerosol and molecular signals [*Shipley et al.*, 1983]. The

318   systematic errors are thus assumed independent for individual lidar measurements in the

319   simulations. This error range is reasonable for most current lidar systems [*Pérez-Ramírez et al.*,

320   2013]. To better understand the impacts of individual input parameters, a systematic error is

321   applied to one input parameter at a time. We repeat the inversion to obtain a new set of aerosol

322   size distribution and CCN$_{retrieved}$ data. For each input parameter and error value, the procedure is

323   repeated with 200 sets of randomly-generated size distributions for each aerosol type. The CCN

324   percentage errors associated with systematic errors can be estimated by comparing retrieved and

325   initial CCN number concentrations as defined above.

326   Figure 4 shows how individual systematic errors impact retrievals. The slope of the curve

327   indicates the sensitivity of CCN errors to systematic errors in individual input parameters. A larger

328 slope implies a higher sensitivity of the CCN retrieval to the systematic error for a given input

329 parameter. In general, retrievals are most sensitive to the errors in α_{355} and α_{532}, and are least

330 sensitive to errors in β_{1064}, with β_{355} and β_{532} falling somewhere in the middle. It is also interesting

331 to note that the results are less sensitive to β_{355}, β_{532}, and β_{1064} at S_cs $\leq 0.10\%$, but are more sensitive

332 to them at S_cs $> 0.10\%$. These results suggest that reducing uncertainties in the extinction

333 coefficients at 355 and 532 nm can effectively improve the CCN retrieval accuracy, while reducing

334 uncertainties in the backscatter coefficients benefits CCN retrievals at higher S_cs. Figure 4 also

335 suggests that the retrieval results are sensitive to the position of the activation radius (denoted by

336 S_c). This effect is the most obvious for Type 2 aerosols. Retrieval uncertainties due to systematic

337 errors in α_{532} are much lower at 0.10% than at other S_cs.

338 In addition, it is also clear that the impact of systematic errors in a given input parameter on

339 CCN retrievals varies with S_c as illustrated by the different signs of the slopes (positive or negative).

340 For example, for Type 3 aerosols, the slopes of α_{355} and β_{355} are negative and positive, respectively,

341 with magnitudes of 0.07% and 0.10%. When S_c exceeds 0.20%, the slopes reverse. These

342 differences most likely result from the reduced sensitivity of the retrieval to the coarse mode of

343 the aerosol size distribution.

344 Furthermore, there are significant differences among the three types of aerosols. Type 3

345 aerosols have the largest absolute CCN errors and Type 1 aerosols have the smallest. These results

346 are consistent with the weights of fine-mode aerosol particles for the three types of aerosols shown

347 in Table 1. These results suggest that there are better constraints for fine-mode aerosols than for

348 coarse-mode aerosols. Therefore, retrieval uncertainties for the coarse mode are higher which

349 introduces larger CCN retrieval errors for aerosols with more weight in the coarse mode, such as

350 Type 3 aerosols. Including additional lidar measurements at wavelengths longer than 1064 nm will

351 reduce the retrieval errors for dust aerosols.

352 **3.4.2 The impact of random errors**

353 Thus far, only the influence of systematic errors on the inversion results has been considered

354 which introduces mean biases in CCN retrievals. Random errors in observations produce random

355 CCN retrieval errors. Random errors are generated by considering a Gaussian distribution centered

356 at zero with a SD equal to 15% of a given input parameter. Random errors are applied to all input

357 optical data simultaneously. For each type of aerosol, we repeat this simulation 5000 times. The

358 statistical results are presented in Fig. 5 and Table 6.

359   At 0.07% and 0.10%, errors in retrieved CCN number concentrations also follow a Gaussian

360   distribution for Type 1 and Type 2 aerosols. When S_c exceeds 0.20%, the Gaussian shape

361   distributions disappear and the high frequencies shift to the edge of the distributions for all types

362   of aerosols. Mean errors are relatively small and non-zero, which is mainly due to the different

363   sensitivities of CCN retrievals to different optical data. These results also reveal that random errors

364   in the input parameters may produce systematic errors in the CCN retrievals. At 0.07%, Type 3

365   aerosols show the largest shift (-20.0%) while Type 2 aerosols have the smallest shift (-1.0% at

366   0.10%). Among the three types of aerosols, the largest errors are found in Type 3 aerosols which

367   contain larger particles. These results are consistent with the sensitivities to the systematic errors,

368   which also have the largest errors for Type 3 aerosols. As discussed earlier, measurements

369   considered in the current multi-wavelength lidar technique contain less information for larger

370   particles. Including additional lidar measurements at longer wavelengths could improve Type 3

371   aerosol retrievals. The maximum values of relative errors decrease with increasing S_cs for all

372   aerosol types (Table 6).

373   **3.4.3 The impact of combined systematic and random errors**

374   In reality, systematic and random errors co-exist in optical input parameters, so their concurrent

375   effects need to be tested. However, for real cases, the input optical data (β_{355}, β_{532}, β_{1064}, α_{355}, α_{532})

376   might be obtained simultaneously from different lidar systems like the Raman lidar or the HSRL

377   with over- or under-estimation of systematic errors appearing in different combinations. For well

378   -designed lidar systems with reliable data processing procedure, it is a good to assume independent

379   systematic errors. However, there do have cases, which can result in dependent systematic errors.

380   For example, near range overlap corrections could introduce dependent systematic errors between

381   355nm extinction and backscattering and 532 nm extinction and backscattering. To simplify the

382   simulation, we only evaluate the overall performance of the new method when systematic and

383   random errors co-exist. The simulations are done by conducting additional simulations with both

384   systematic and random errors occurring simultaneously. Systematic errors are randomly assigned

385   a sign (over/underestimation) as was done by *Pérez-Ramírez et al.* [2013]. Systematic errors are

386   difficult to reveal, whereas random errors can be revealed and reduced by repeating the

387   measurements. Systematic errors of 0–20% with a step width of 5% are added to all optical input

388   parameters (β_{355}, β_{532}, β_{1064}, α_{355}, α_{532}) concurrently. As for random errors, they are generated by

389 considering a Gaussian distribution centered at zero with a SD equal to 5% of a given input
390 parameter. For each type of aerosol, simulations were performed 500 times. The CCN retrieval
391 results are presented in Fig. 6 and Table 7.

392 For Type 3 aerosols, the largest mean CCN error is 25.8% at $S_c = 0.07\%$. For Type 1 and Type
393 2 aerosols, mean CCN errors in all cases are less than 10.3%. These retrieved CCN errors are much
394 smaller than those obtained in Section 3.4.1 when only the systematic error was considered at each
395 wavelength independently. Adding errors for multiple optical input parameters simultaneously
396 might compensate each other and improve the CCN retrievals. However, the SDs are larger with
397 maximum values reaching 20.5%, 26.7%, and 53.1% for Type 1, Type 2, and Type 3 aerosols,
398 respectively, due to the very large measurement errors created by the random combination of
399 systematic and random errors.

400 **4. A real case study**

401 The evaluation of CCN retrievals depends critically on how well lidar and in situ measurements
402 are matched, as matching errors can become overwhelming. Due to a lack of collocated
403 measurements of the required quantities, we have not yet seen any evaluation done using real-case
404 data. It is done here by comparing CCN derived from lidar measurements and measured by a Cloud
405 Condensation Nuclei counter (CCNc) on the ground on 16 August 2015 at the U.S. Department of
406 Energy's Atmospheric Radiation Measurement (ARM) Climate Research Facility Southern Great
407 Plains (SGP) site.

408 Multi-wavelength lidar data were collected during the Combined HSRL and Raman lidar
409 Measurement Study (CHARMS) intensive observation period (IOP) that occurred in August 2015
410 at the SGP site [*Ferrare et al.*, 2017]. During the CHARMS IOP, aerosol backscatter profiles at
411 532 and 1064 nm, and aerosol extinct-ion profiles at 532 nm were acquired from the University of
412 Wisconsin HSRL located at the SGP site. HSRL aerosol profiles, when combined with aerosol
413 backscatter and extinction profiles at 355 nm collected by the SGP Raman lidar, provide a full set
414 of three aerosol backscatter (355, 532, and 1064 nm) and two aerosol extinction (355 and 532 nm)
415 profiles for CCN retrievals. CHARMS data were processed at temporal and vertical resolutions of
416 10 minutes and 0.06 kilometers, respectively. To avoid the impact of the overlap function on
417 extinction and backscattering retrievals, the lower limit of the height range where CCN properties
418 are retrieved from optical data is 0.6 km above ground level. We also set the upper limit of the
419 retrieval height range as 3 km due to the low aerosol loading in higher layers. For comparison

420 purposes, in situ CCN concentrations under different supersaturation conditions (S_cs ranging from

421 0.1–0.75%) were measured on the ground by the CCNc at the same site.

422 Although the SGP site is located in a rural area surrounded by cattle pastures and agricultural

423 fields, air masses transported from the south and southeast often arrive at this site in the summer

424 [*Mahish and Collins*, 2017]. Based on an overview of aerosol-type-dependent properties from

425 more than 10 years of lidar observations [*Baars et al.*, 2016] and Fig. 7, we can infer that aerosols

426 in this case are not dust but urban or biomass burning aerosols by virtue of the lidar ratio (Fig. 7a),

427 the depolarization ratio (Fig. 7b) and the Ångström exponent (Fig. 7c). The aerosol depolarization

428 ratio was less than 0.1 on this day, which indicates that using the Mie theory for CCN retrievals is

429 reasonable although potential systematic errors introduced by irregular-shaped aerosols are not

430 negligible. To further distinguish between these two aerosol types, 48-h back trajectories

431 calculated using the Hybrid Single-Particle Lagrangian Integrated Trajectory model [*Draxler and*

432 *Rolph*, 2003] and active fire spots from Moderate Resolution Imaging Spectroradiometer (MODIS)

433 data [*Giglio et al.*, 2016] on 15 August 2015 are also used. Fig. 8a and Fig. 8b show that aerosols

434 on 16 August 2015 originated from fire activities in the southeast and northeast of the SGP site.

435 Therefore, the aerosol loading in this case was greatly influenced by biomass-burning aerosols

436 transported to the SGP site. Based on the analysis of a multi-year record of hygroscopic

437 measurements made at the SGP site [*Mahish and Collins*, 2017], a simplified hygroscopicity

438 parameter κ equal to 0.2 is chosen for CCN retrievals here. This value falls within the reasonable

439 range of κ for biomass-burning aerosols [*Petters et al.*, 2009].

440 Total particle number concentrations (condensation nuclei, CN) retrievals from the lidar are

441 shown in Fig. 9. Fig. 9a shows the temporal evolution of the vertical profile of aerosol extinction

442 at 355 nm in the 0.6–3 km height ranging from 0000 universal coordinated time (UTC) to 2400

443 UTC on 16 August 2015. During that day, a distinct aerosol layer was observed near the ground

444 with an extinction coefficient of up to 0.25 km^{-1}. From 1200–2400 UTC, the aerosol layer

445 increased in altitude up to 2.2 km due to the enhancement of turbulent mixing in the atmosphere.

446 Above that layer, several weak aerosol layers appeared and aerosols were distributed more

447 uniformly with height. The CN number concentrations which is computed from the retrieved size

448 distribution parameters are shown in Fig. 9b.

449 Based on an investigation of the spatio-temporal distributions of *RH* at SGP during that day,

450 the maximum *RH* is lower than 70% at each height and lower than 60% at 0.6 km, which didn't

451 reach the deliquescence *RH* of biomass burning aerosols [*Lei et al.*, 2014; *Kuang et al.*, 2016].

452 Thus the aerosol size distributions used for estimating CCN number concentrations are little

453 influenced by aerosol hygroscopic growth on that day. For a comparison with surface in-situ

454 measurements, retrieved CCN number concentrations are calculated using Eq. (7) with time-

455 dependent supersaturations set for the in situ CCNc. Figure 10 shows the spatio-temporal

456 distributions of CCN number concentrations (Fig. 10a), the time series of lidar-retrieved and

457 surface-measured CCN concentrations (Fig. 10b) and a scatterplot of surface-measured CCN

458 concentrations as a function of lidar-retrieved CCN concentration (Fig. 10c) respectively. Lidar

459 retrievals shown in Fig. 10b and Fig. 10c are within a height range of 0.6 km. Figure 10a shows

460 that the retrieved CCN number concentrations are roughly constant with height in the boundary

461 layer except for the CCN number concentrations around 15:00 (UTC) that is likely due to the

462 atmospheric transportation. The time series shows that both instruments generally captured the

463 temporal evolution of CCN concentration on that day at the SGP site (Fig. 10b). However, periods

464 with substantially different CCN concentrations were also observed. For example, higher CCN

465 concentrations at ground level than at 0.6 km in the evening and overnight (0000–1000 UTC) are

466 seen, most likely due to the vertically inhomogeneous distribution of aerosols. Figure 10c shows

467 that CCN concentrations derived from measurements made by both instruments were well

468 correlated. The correlation coefficient is 0.57 and the regression slope is 1.06 with most points

469 lying close to the 1:1 line. Other than the vertical inhomogeneity of the atmosphere, most of the

470 remaining differences could be due to the different observation methods and the extinction and

471 backscattering retrieval uncertainties from the two lidar systems. Although a detailed uncertainty

472 analysis is still needed and will be done in a future study, this comparison demonstrates the

473 potential of using multi-wavelength Raman lidar measurements to profile aerosol and CCN

474 properties.

5. Conclusions

476 We have investigated the feasibility of retrieving CCN number concentrations using multi-

477 wavelength HSRL and Raman lidar measurements. Three representative types of aerosols with

478 bimodal size distributions retrieved from AERONET observations were considered, namely, urban

479 industrial (Type 1), biomass burning (Type 2), and dust (Type 3). The aerosol types are assumed

480 known and provide the mean complex refractive index. This leaves six size parameters to retrieve.

481 To avoid the ill-posed inversion problem, the mode width of the coarse mode is assumed.

482 Sensitivity tests suggest that this assumption only introduces a small error in the retrieval results.

483 The retrieval is implemented based on LUTs generated from Mie scattering calculations. A

484 successive approximation method in two steps is utilized as a tradeoff between the accuracy and

485 computation time of the inversion. Once the parameters of the aerosol size distribution are obtained

486 through the LUT, CCN number concentrations can be estimated.

487 Numerical simulations were performed to evaluate the algorithm performance with and

488 without errors in the extinction and backscatter coefficients. For error-free input, CCN

489 concentrations for the three types of aerosols were well reproduced with good accuracy and

490 stability. Simulations with systematic errors show that the uncertainties of extinction coefficients

491 at 355 and 532 nm have a higher impact on the retrieval results, and that retrievals are more

492 dependent on the uncertainties in backscatter coefficients at higher S_cs than at lower S_cs. There are

493 significant differences in retrieval uncertainties among the three types of aerosols due to the

494 different weights of fine- and coarse-mode aerosol particles among them. The differences can be

495 explained by the weaker constraint of the algorithm for the coarse mode of aerosol particles than

496 for the fine mode of particles. Tests where 15% random errors were considered were done next.

497 CCN number concentrations had Gaussian distributions at lower S_cs (0.07%, 0.10%) for all types

498 of aerosols except for Type 3. This distribution shape disappeared at higher S_cs. Simulations with

499 both random and systematic errors, which represent more realistic cases, show that both errors

500 together improved mean CCN retrievals because random and systematic errors often offset each

501 other. Simulations showed that if the input optical data had a 15% systematic error and a 5%

502 random error simultaneously, CCN number concentrations were retrieved with an accuracy of -

503 $3.3 \pm 18.7\%$ for urban industrial aerosols, $-7.6 \pm 15.3\%$ for biomass burning aerosols, and $-24.9 \pm$

504 48.3% for dust aerosols at $S_c = 0.07\%$.

505 The focus of the numerical simulations is to explore the sensitivity of CCN retrievals to errors

506 in the measurements of extinction and backscatter coefficients. The influences of aerosol hydration

507 and dynamic mixing on the refractive index are not considered in the simulations. When processing

508 observational data, the impact of relative humidity needs to be accounted for since the lidars

509 retrieve the wet size distributions while the CCN calculations require the dry size distribution.

510 From Raman lidar measurements, temperature and water vapor below clouds can be determined

511 to provide the vertical profile of relative humidity [*Ferrare*, 2000; *Behrendt et al.*, 2002; *Reichardt*

512 *et al.*, 2012]. Aerosol-type-dependent hygroscopic growth may thus be needed to estimate the dry

size distribution from the wet size distribution and *RH* for CCN calculations. Furthermore, relative humidity information can be used to adjust the mean reflective index for the LUT. The impacts of humidity and the non-spherical dust shape will be studied and implemented, if warranted, in future algorithm development.

The algorithm was applied to observational data from the ARM Climate Research Facility SGP site to illustrate the potential of the algorithm. For the first time, lidar-retrieved CCN concentrations were compared with simultaneous measurements from an in situ CCNc. Considering the vertical aerosol inhomogeneity between the surface and 0.6 km above ground level, CCN concentrations from in situ measurements and lidar retrievals agree well.

The study demonstrates the potential of using multi-wavelength Raman lidar measurements to profile aerosol and CCN properties. The height-dependent information of aerosols and CCN are important for investigating the aerosol indirect effect in climate models. To ensure retrieval accuracy, 355 and 532 nm extinction coefficients need to be reliably derived. It is also important to consider including measurements made at longer wavelengths to improve CCN retrievals for dust aerosols.

References

Andreae, M. O. (2009), Correlation between cloud condensation nuclei concentration and aerosol optical thickness in remote and polluted regions, *Atmos. Chem. Phys.*, *9*(2), 543–556, doi:10.5194/acp-9-543-2009.

Ansmann, A., M. Riebesell, U. Wandinger, C. Weitkamp, E. Voss, W. Lahmann, and W. Michaelis (1992), Combined raman elastic-backscatter LIDAR for vertical profiling of moisture, aerosol extinction, backscatter, and LIDAR ratio, *Appl. Phys. B*, *55*(1), 18–28, doi:10.1007/BF00348608.

Baars, H., et al. (2016), An overview of the first decade of PollyNET: an emerging network of automated Raman-polarization lidars for continuous aerosol profiling, *Atmos. Chem. Phys.*, *16*(8), 5111–5137, doi:10.5194/acp-16-5111-2016.

Behrendt, A., T. Nakamura, M. Onishi, R. Baumgart, and T. Tsuda (2002), Combined Raman lidar for the measurement of atmospheric temperature, water vapor, particle extinction coefficient, and particle backscatter coefficient, *Appl. Opt.*, *41*(36), 7657–7666, doi:10.1364/AO.41.007657.

Boucher, O., D. Randall, P. Artaxo, C. Bretherton, G. Feingold, P. Forster, V.-M. Kerminen, Y. Kondo, H. Liao, and U. Lohmann (2013), Clouds and aerosols, in *Climate change 2013: The physical science basis. Contribution of working group I to the fifth assessment report of the intergovernmental panel on climate change*, edited by T. F. Stocker et al., pp. 571–657, Cambridge University Press.

Burkart, J., G. Steiner, G. Reischl, and R. Hitzenberger (2011), Long-term study of cloud condensation nuclei (CCN) activation of the atmospheric aerosol in Vienna, *Atmos. Environ.*, *45*(32), 5751–5759, doi:10.1016/j.atmosenv.2011.07.022.

Burton, S. P., R. A. Ferrare, C. A. Hostetler, J. W. Hair, R. R. Rogers, M. D. Obland, C. F. Butler, A. L. Cook, D. B. Harper, and K. D. Froyd (2012), Aerosol classification using airborne High Spectral Resolution Lidar measurements – methodology and examples, *Atmos. Meas. Tech.*, *5*(1), 73–98, doi:10.5194/amt-5-73-2012.

Cai, Y., D. C. Montague, W. Mooiweer-Bryan, and T. Deshler (2008), Performance characteristics of the ultra high sensitivity aerosol spectrometer for particles between 55 and 800 nm: Laboratory and field studies, *J. Aerosol Sci.*, *39*, 759–769, doi:10.1016/j.jaerosci.2008.04.007.

Carslaw, K. S., O. Boucher, D. V. Spracklen, G. W. Mann, J. G. L. Rae, S. Woodward, and M. Kulmala (2010), A review of natural aerosol interactions and feedbacks within the Earth system, *Atmos. Chem. Phys., 10*(4), 1701–1737, doi:10.5194/acp-10-1701-2010.

Chemyakin, E., D. Müller, S. Burton, A. Kolgotin, C. Hostetler, and R. Ferrare (2014), Arrange and average algorithm for the retrieval of aerosol parameters from multiwavelength high-spectral-resolution lidar/Raman lidar data, *Appl. Opt., 53*(31), 7252–7266, doi:10.1364/AO.53.007252.

Chemyakin, E., S. Burton, A. Kolgotin, D. Müller, C. Hostetler, and R. Ferrare (2016), Retrieval of aerosol parameters from multiwavelength lidar: investigation of the underlying inverse mathematical problem, *Appl. Opt., 55*(9), 2188–2202, doi:10.1364/AO.55.002188.

Chen, G., et al. (2011), Observations of Saharan dust microphysical and optical properties from the Eastern Atlantic during NAMMA airborne field campaign, *Atmos. Chem. Phys., 11*(2), 723–740, doi:10.5194/acp-11-723-2011.

Deng, Z. Z., C. Zhao, N. Ma, P. Liu, L. Ran, W. Xu, J. Chen, Z. Liang, S. Liang, M. Huang (2011), Size-resolved and bulk activation properties of aerosols in the North China Plain, *Atmos. Chem. Phys., 11*(8), 3835–3846, doi:10.5194/acp-11-3835-2011.

Draxler, R. R., and G. Rolph (2003), HYSPLIT (HYbrid Single-Particle Lagrangian Integrated Trajectory) model access via NOAA ARL READY website (http://www.arl.noaa. gov/ready/hysplit4. html). NOAA Air Resources Laboratory, Silver Spring, edited, Md.

Dubovik, O., B. Holben, T. F. Eck, A. Smirnov, Y. J. Kaufman, M. D. King, D. Tanré, and I. Slutsker (2002), Variability of absorption and optical properties of key aerosol types observed in worldwide locations, *J. Atmos. Sci., 59*(3), 590–608, doi:10.1175/1520-0469(2002)059<0590:VOAAOP>2.0.CO;2.

Dusek, U., et al. (2006), Size matters more than chemistry for cloud-nucleating ability of aerosol particles, *Science, 312*(5778), 1375–1378, doi:10.1126/science.1125261.

Fan, J., Y. Wang, D. Rosenfeld, and X. Liu (2016), Review of Aerosol–Cloud Interactions: Mechanisms, Significance, and Challenges, *J. Atmos. Sci., 73*(11), 4221–4252, doi:10.1175/JAS-D-16-0037.1.

Ferrare, R. A. (2000), Raman lidar profiling of water vapor and aerosols over the ARM SGP site, *Rep.*, Brookhaven National Lab., Upton, NY (US).

600 Ferrare, R. A. (2017), Characterizing the vertical distribution of aerosols above SGP using

601   CHARMS data, ARM/ASR PI Meeting.

602 Feingold, G., and C. J. Grund (1994), Feasibility of using multiwavelength lidar measurements to

603   measure cloud condensation nuclei, *J. Atmos. Ocean. Tech.*, *11*(6), 1543–1558,

604   doi:10.1175/1520-0426(1994)011<1543:FOUMLM>2.0.CO;2.

605 Feingold, G., S. Yang, R. Hardesty, and W. Cotton (1998), Feasibility of retrieving cloud

606   condensation nucleus properties from Doppler cloud radar, microwave radiometer, and lidar, *J.*

607   *Atmos. Ocean. Tech.*, *15*(5), 1188–1195, doi:10.1175/1520-

608   0426(1998)015<1188:FORCCN>2.0.CO;2.

609 Fitzgerald, J. W. (1973), Dependence of the supersaturation spectrum of CCN on aerosol size

610   distribution and composition, *J. Atmos. Sci.*, *30*(4), 628–634, doi:10.1175/1520-

611   0469(1973)030<0628:DOTSSO>2.0.CO;2.

612 Ghan, S. J., and D. R. Collins (2004), Use of in situ data to test a Raman lidar-based cloud

613   condensation nuclei remote sensing method, *J. Atmos. Ocean. Tech.*, *21*(2), 387–394,

614   doi:10.1175/1520-0426(2004)021<0387:UOISDT>2.0.CO;2.

615 Ghan, S. J., T. A. Rissman, R. Elleman, R. A. Ferrare, D. Turner, C. Flynn, J. Wang, J. Ogren, J.

616   Hudson, and H. H. Jonsson (2006), Use of in situ cloud condensation nuclei, extinction, and

617   aerosol size distribution measurements to test a method for retrieving cloud condensation nuclei

618   profiles from surface measurements, *J. Geophys. Res. Atmos.*, *111*(D5),

619   doi:10.1029/2004JD005752.

620 Giglio, L., W. Schroeder, and C. O. Justice (2016), The collection 6 MODIS active fire detection

621   algorithm and fire products, *Rem. Sens. Environ.*, *178*, 31–41, doi: 10.1016/j.rse.2016.02.054.

622 Granados-Muñoz, M., F. Navas-Guzmán, J. Bravo-Aranda, J. Guerrero-Rascado, H. Lyamani, A.

623   Valenzuela, G. Titos, J. Fernández-Gálvez, and L. Alados-Arboledas (2015), Hygroscopic

624   growth of atmospheric aerosol particles based on active remote sensing and radiosounding

625   measurements: selected cases in southeastern Spain, *Atmos. Meas. Tech.*, *8*(2), 705-718.

626 Grandey, B., and P. Stier (2010), A critical look at spatial scale choices in satellite-based aerosol

627   indirect effect studies, *Atmos. Chem. Phys.*, *10*(23), 11459–11470, doi:10.5194/acp-10-11459-

628   2010.

Groß, S., M. Esselborn, B. Weinzierl, M. Wirth, A. Fix, and A. Petzold (2013), Aerosol classification by airborne high spectral resolution lidar observations, *Atmos. Chem. Phys.*, *13*(5), 2487–2505, doi:10.5194/acp-13-2487-2013.

Gryspeerdt, E., P. Stier, and D. Partridge (2014), Satellite observations of cloud regime development: the role of aerosol processes, *Atmos. Chem. Phys.*, *14*(3), 1141–1158, doi:10.5194/acp-14-1141-2014.

Horvath, H., R. Gunter, and S. Wilkison (1990), Determination of the coarse mode of the atmospheric aerosol using data from a forward-scattering spectrometer probe, *Aerosol Sci. Tech.*, *12*(4), 964–980, doi:10.1080/02786829008959407.

Junge, C. (1952), Gesetzmäßigkeiten in der größenverteilung atmosphärischer aerosole über dem kontinent, *Berichte des deutschen Wetterdienstes*, *35*, 261–277.

Junge, C., and E. McLaren (1971), Relationship of cloud nuclei spectra to aerosol size distribution and composition, *J. Atmos. Sci.*, *28*(3), 382–390, doi:10.1175/1520-0469(1971)028<0382:ROCNST>2.0.CO;2.

Jurányi, Z., M. Gysel, E. Weingartner, P. F. DeCarlo, L. Kammermann, and U. Baltensperger (2010), Measured and modelled cloud condensation nuclei number concentration at the high alpine site Jungfraujoch, *Atmos. Chem. Phys.*, *10*(16), 7891–7906, doi:10.5194/acp-10-7891-2010.

Kantorovitch, L. (1939), The method of successive approximation for functional equations, *Acta Mathematica*, *71*(1), 63–97, doi:10.1007/BF02547750.

Koehler, K., S. Kreidenweis, P. DeMott, M. Petters, A. Prenni, and C. Carrico (2009), Hygroscopicity and cloud droplet activation of mineral dust aerosol, *Geophys. Res. Lett.*, *36*(8), doi:10.1029/2009GL037348.

Koren, I., L. A. Remer, Y. J. Kaufman, Y. Rudich, and J. V. Martins (2007), On the twilight zone between clouds and aerosols, *Geophys. Res. Lett.*, *34*(8), doi:10.1029/2007GL029253.

Kuang, Y., C. S. Zhao, N. Ma, H. J. Liu, Y. X. Bian, J. C. Tao, and M. Hu (2016), Deliquescent phenomena of ambient aerosols on the North China Plain, *Geophys. Res. Lett.*, *43*, 8744–8750, doi:10.1002/2016GL070273.

Lei, T., A. Zuend, W. Wang, Y. Zhang, and M. Ge (2014), Hygroscopicity of organic compounds from biomass burning and their influence on the water uptake of mixed organic ammonium sulfate aerosols, *Atmos. Chem. Phys.*, *14*(20), 11165-11183.

660 Li, J., Y. Yin, P. Li, Z. Li, R. Li, M. Gribb, Z. Dong, F. Zhang, J. Li, G. Ren, L. Jin, and Y. Li
661   (2015a), Aircraft measurements of the vertical distribution and activation property of aerosol
662   particles over the Loess Plateau in China, *Atmos. Res.*, *155*, 73–86,
663   doi:10.1016/j.atmosres.2014.12.004.

664   Li, J., X. Liu, L. Yuan, Y. Yin, Z. Li, P. Li, G. Ren, L. Jin, R. Li, Z. Dong, Y. Li, and J. Yang
665   (2015b), Vertical distribution of aerosol optical properties based on aircraft measurements over
666   the Loess Plateau in China, *J. Environ. Sci.*, *34*, 44–56, doi:10.1016/j.jes.2015.01.021.

667   Liu, J., and Z. Li (2014), Estimation of cloud condensation nuclei concentration from aerosol
668   optical quantities: influential factors and uncertainties, *Atmos. Chem. Phys.*, *14*(1), 471–483,
669   doi:10.5194/acp-14-471-2014.

670 Liu, J., P. Yang, and K. Muinonen (2015), Dust-aerosol optical modeling with Gaussian spheres:
671   Combined invariant-imbedding T-matrix and geometric-optics approach, *J. Quant. Spectrosc.*
672   *Radiat. Transf.*, *161*, 136–144, doi:10.1016/j.jqsrt.2015.04.003.

673   Liu, P., C. Zhao, T. Göbel, E. Hallbauer, A. Nowak, L. Ran, W. Xu, Z. Deng, N. Ma, and K.
674   Mildenberger (2011), Hygroscopic properties of aerosol particles at high relative humidity and
675   their diurnal variations in the North China Plain, *Atmos. Chem. Phys.*, *11*(7), 3479–3494,
676   doi:10.5194/acp-11-3479-2011.

677   Luo, T., Z. Wang, R. A. Ferrare, C. A. Hostetler, R. Yuan, and D. Zhang (2015), Vertically
678   resolved separation of dust and other aerosol types by a new lidar depolarization method, *Opt.*
679   *Express, 23*(11), 14095-14107, doi:10.1364/OE.23.014095.

680 Lv, M., D. Liu, Z. Li, J. Mao, Y. Sun, Z. Wang,Y. Wang and C. Xie (2017), Hygroscopic growth
681   of atmospheric aerosol particles based on lidar, radiosonde, and in situ measurements: case
682   studies from the Xinzhou field campaign, *J. Quan. Spectrosc. Ra.*, *188*, 60-70,
683   doi:10.1016/j.jqsrt.2015.12.029.

684 Mahish, M., and D. Collins (2017), Analysis of a multi-year record of size-resolved hygroscopicity
685   measurements from a rural site in the US, *Aerosol Air Qual. Res.*, *17*, 1489–1500,
686   doi:10.4209/aaqr.2016.10.0443.

687   Malloy, Q. G., S. Nakao, L. Qi, R. Austin, C. Stothers, H. Hagino, and D. R. Cocker III (2009),
688   Real-time aerosol density determination utilizing a modified scanning mobility particle sizer—
689   aerosol particle mass analyzer system, *Aerosol Sci. Tech.*, *43*(7), 673–678, doi:
690   10.1080/02786820902832960.

Mamouri, R.-E., and A. Ansmann (2016), Potential of polarization lidar to provide profiles of CCN-and INP-relevant aerosol parameters, *Atmos. Chem. Phys.*, *16*(9), 5905–5931, doi: 10.5194/acp-16-5905-2016.

Müller, D., U. Wandinger, and A. Ansmann (1999), Microphysical particle parameters from extinction and backscatter lidar data by inversion with regularization: theory, *Appl. Opt.*, *38*(12), 2346–2357, doi:10.1364/AO.38.002346.

Müller, D., F. Wagner, U. Wandinger, A. Ansmann, M. Wendisch, D. Althausen, and W. von Hoyningen-Huene (2000), Microphysical particle parameters from extinction and backscatter lidar data by inversion with regularization: experiment, *Appl. Opt.*, *39*(12), 1879–1892, doi:10.1364/AO.39.001879.

Müller, D., C. A. Hostetler, R. A. Ferrare, S. P. Burton, E. Chemyakin, A. Kolgotin, J. W. Hair, A. L. Cook, D. B. Harper, R. R. Rogers, R. W. Hare, C. S. Cleckner, M. D. Obland, J. Tomlinson, L. K. Berg, B. Schmid (2014), Airborne Multiwavelength High Spectral Resolution Lidar (HSRL-2) observations during TCAP 2012: vertical profiles of optical and microphysical properties of a smoke/urban haze plume over the northeastern coast of the US, *Atmos. Meas. Tech.*, *7*(10), 3487–3496, doi:10.5194/amt-7-3487-2014.

Nenes, A., P. Y. Chuang, R. C. Flagan, and J. H. Seinfeld (2001), A theoretical analysis of cloud condensation nucleus (CCN) instruments, *J. Geophys. Res. Atmos.*, *106*(D4), 3449–3474, doi: 10.1029/2000JD900614.

Nousiainen, T. (2009), Optical modeling of mineral dust particles: A review, *J. Quant. Spectrosc. Radiat. Transf.*, *110*(14), 1261–1279, doi:10.1016/j.jqsrt.2009.03.002.

Paasonen, P., et al. (2013), Warming-induced increase in aerosol number concentration likely to moderate climate change, *Nature Geosci,* *6*(6), 438–442, doi:10.1038/ngeo1800.

Paramonov, M., P. P. Aalto, A. Asmi, N. Prisle, V. M. Kerminen, M. Kulmala, and T. Petäjä (2013), The analysis of size-segregated cloud condensation nuclei counter (CCNC) data and its implications for cloud droplet activation, *Atmos. Chem. Phys.*, *13*(20), 10285–10301, doi:10.5194/acp-13-10285-2013.

Pérez-Ramírez, D., D. Whiteman, I. Veselovskii, A. Kolgotin, M. Korenskiy, and L. Alados-Arboledas (2013), Effects of systematic and random errors on the retrieval of particle microphysical properties from multiwavelength lidar measurements using inversion with regularization, *Atmos. Meas. Tech.*, *6*, 3039–3054, doi:10.5194/amt-6-3039-2013.

Peters, T. M., and D. Leith (2003), Concentration measurement and counting efficiency of the aerodynamic particle sizer 3321, *J. Atmos. Sci.*, *34*(5), 627–634, doi:10.1016/S0021-8502(03)00030-2.

Petters, M. D., and S. M. Kreidenweis (2007), A single parameter representation of hygroscopic growth and cloud condensation nucleus activity, *Atmos. Chem. Phys.*, *7*(8), 1961–1971, doi:10.5194/acp-7-1961-2007.

Petters, M. D., C. M. Carrico, S. M. Kreidenweis, A. J. Prenni, P. J. DeMott, J. L. Collett, and H. Moosmueller (2009), Cloud condensation nucleation activity of biomass burning aerosol, *J. Geophys. Res. Atmos.*, *114*(D22), doi:10.1029/2009JD012353.

Reichardt, J., U. Wandinger, V. Klein, I. Mattis, B. Hilber, and R. Begbie (2012), RAMSES: German Meteorological Service autonomous Raman lidar for water vapor, temperature, aerosol, and cloud measurements, *Appl. Opt.*, *51*(34), 8111–8131, doi:10.1364/AO.51.008111.

Remer, L. A., Y. J. Kaufman, D. Tanré, S. Mattoo, D. A. Chu, J. V. Martins, R. R. Li, C. Ichoku, R. C. Levy, R. G. Kleidman, T. F. Eck, E. Vermote, and B. N. Holben (2005), The MODIS aerosol algorithm, products, and validation, *J. Atmos. Sci.*, *62*(4), 947–973, doi:10.1175/JAS3385.1.

Roberts, G. C., and A. A. Nenes (2005), Continuous-flow streamwise thermal-gradient CCN chamber for atmospheric measurements, *Aerosol Sci. Tech.*, *39*(3), 206–221, doi: 10.1080/027868290913988.

Rosenfeld, D., W. L. Woodley, A. Lerner, G. Kelman, and D. T. Lindsey (2008), Satellite detection of severe convective storms by their retrieved vertical profiles of cloud particle effective radius and thermodynamic phase, *J. Geophys. Res. Atmos.*, *113*(D4), doi:10.1029/2007JD008600.

Rosenfeld, D., et al. (2016), Satellite retrieval of cloud condensation nuclei concentrations by using clouds as CCN chambers, *Proc. Natl. Acad. Sci. U. S. A.*, *113*(21), 5828–5834, doi:10.1073/pnas.1514044113.

Schuster, G. L., O. Dubovik, and B. N. Holben (2006), Angstrom exponent and bimodal aerosol size distributions, *J. Geophys. Res. Atmos.*, *111*(D7), doi:10.1029/2005JD006328.

Shinozuka, Y., A. D. Clarke, A. Nenes, A. Jefferson, R. Wood, C. S. McNaughton, J. Ström, P. Tunved, J. Redemann, K. L. Thornhill, R. H. Moore, T. L. Lathem, J. J. Lin and Y. J. Yoon (2015), The relationship between cloud condensation nuclei (CCN) concentration and light extinction of dried particles: indications of underlying aerosol processes and implications for

satellite-based CCN estimates, *Atmos. Chem. Phys.*, *15*(13), 7585–7604, doi:10.5194/acp-15-7585-2015.

Shipley, S. T., D. Tracy, E. W. Eloranta, J. T. Trauger, J. Sroga, F. Roesler, and J. A. Weinman (1983), High spectral resolution lidar to measure optical scattering properties of atmospheric aerosols. 1: Theory and instrumentation, *Appl. Opt.*, *22*(23), 3716–3724.

Veselovskii, I., A. Kolgotin, V. Griaznov, D. Müller, U. Wandinger, and D. N. Whiteman (2002), Inversion with regularization for the retrieval of tropospheric aerosol parameters from multiwavelength lidar sounding, *Appl. Opt.*, *41*(18), 3685–3699, doi:10.1364/AO.41.003685.

Veselovskii, I., A. Kolgotin, V. Griaznov, D. Müller, K. Franke, and D. N. Whiteman (2004), Inversion of multiwavelength Raman lidar data for retrieval of bimodal aerosol size distribution, *Appl. Opt.*, *43*(5), 1180–1195, doi:10.1364/AO.43.001180.

Veselovskii, I., D. Whiteman, A. Kolgotin, E. Andrews, and M. Korenskii (2009), Demonstration of aerosol property profiling by multiwavelength lidar under varying relative humidity conditions, *J. Atmos. Ocean. Tech.*, *26*(8), 1543-1557.

Veselovskii, I., D. Whiteman, M. Korenskiy, A. Kolgotin, O. Dubovik, and D. Pérez-Ramírez (2013), Retrieval of height-temporal distributions of particle parameters from multiwavelength lidar measurements using linear estimation technique and comparison results with AERONET, *Atmos. Meas. Tech.*, *6*, 2671–2682, doi:10.5194/amt-6-2671-2013.

Wandinger, U. (2005), Raman lidar techniques for the observation of atmospheric aerosols, temperature, and humidity, paper presented at 13th International School on Quantum Electronics: Laser Physics and Applications, International Society for Optics and Photonics.

Wang, Y., F. Zhang, Z. Li, H. Tan, H. Xu, J. Ren, J. Zhao, W. Du, and Y. Sun (2017), Enhanced hydrophobicity and volatility of submicron aerosols under severe emission control conditions in Beijing, *Atmos. Chem. Phys., 17*(8), 5239–5251, doi:10.5194/acp-17-5239-2017.

Wang, Y., Z. Li, Y. Zhang, W. Du, F. Zhang, H. Tan, H. Xu, X. Jin, X. Fan, Z. Dong, Q. Wang, Y. Sun (2018), Characterization of aerosol hygroscopicity, mixing state, and CCN activity at a suburban site in the central North China Plain, *Atmos. Chem. Phys. Discuss.*, 1–34.

Zhang, F., Y. Li, Z. Li, L. Sun, R. Li, C. Zhao, P. Wang, Y. Sun, X. Liu, J. Li, P. Li, G. Ren, and T. Fan (2014), Aerosol hygroscopicity and cloud condensation nuclei activity during the AC3Exp campaign: implications for cloud condensation nuclei parameterization, *Atmos. Chem. Phys.*, *14*(24), 13423–13437, doi:10.5194/acp-14-13423-2014.
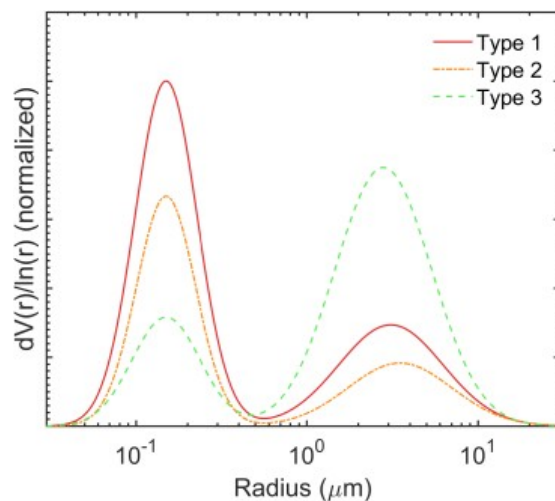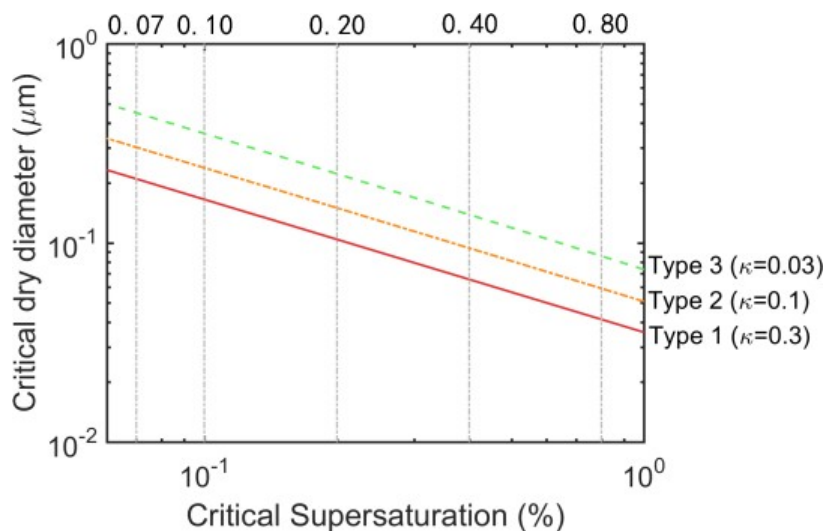
786 **Figure 1.** Normalized size distributions representing the three types of aerosols considered in this

787 study. Types 1–3 represent urban industrial, biomass burning, and dust aerosols, respectively.
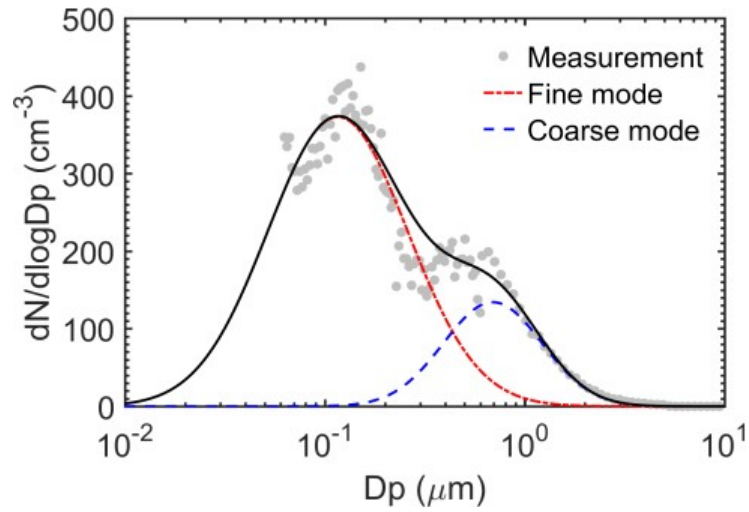
788

789

790 **Figure 2.** The relationship between particle critical dry diameter and critical supersaturation ratio

791   for Type 1 (κ = 0.3), Type 2 (κ = 0.1), and Type 3 (κ = 0.01) aerosols. The parameter κ is the

792 hygroscopicity parameter. Gray dashed lines denote the five critical S_cs for activation (0.07, 0.10,

793 0.20, 0.40, and 0.80%).

794

795

Figure 3. Observed particle number size distribution measured on 20 August 2006 during the NAMMA field campaign. Particle size is represented by the geometric diameter. Solid dots denote integrated UHSAS and APS measurements. Curves are bimodal lognormal fits for the size distributions of the fine mode (red dash-dotted line), the coarse mode (blue dashed line) and the full mode (black solid line).
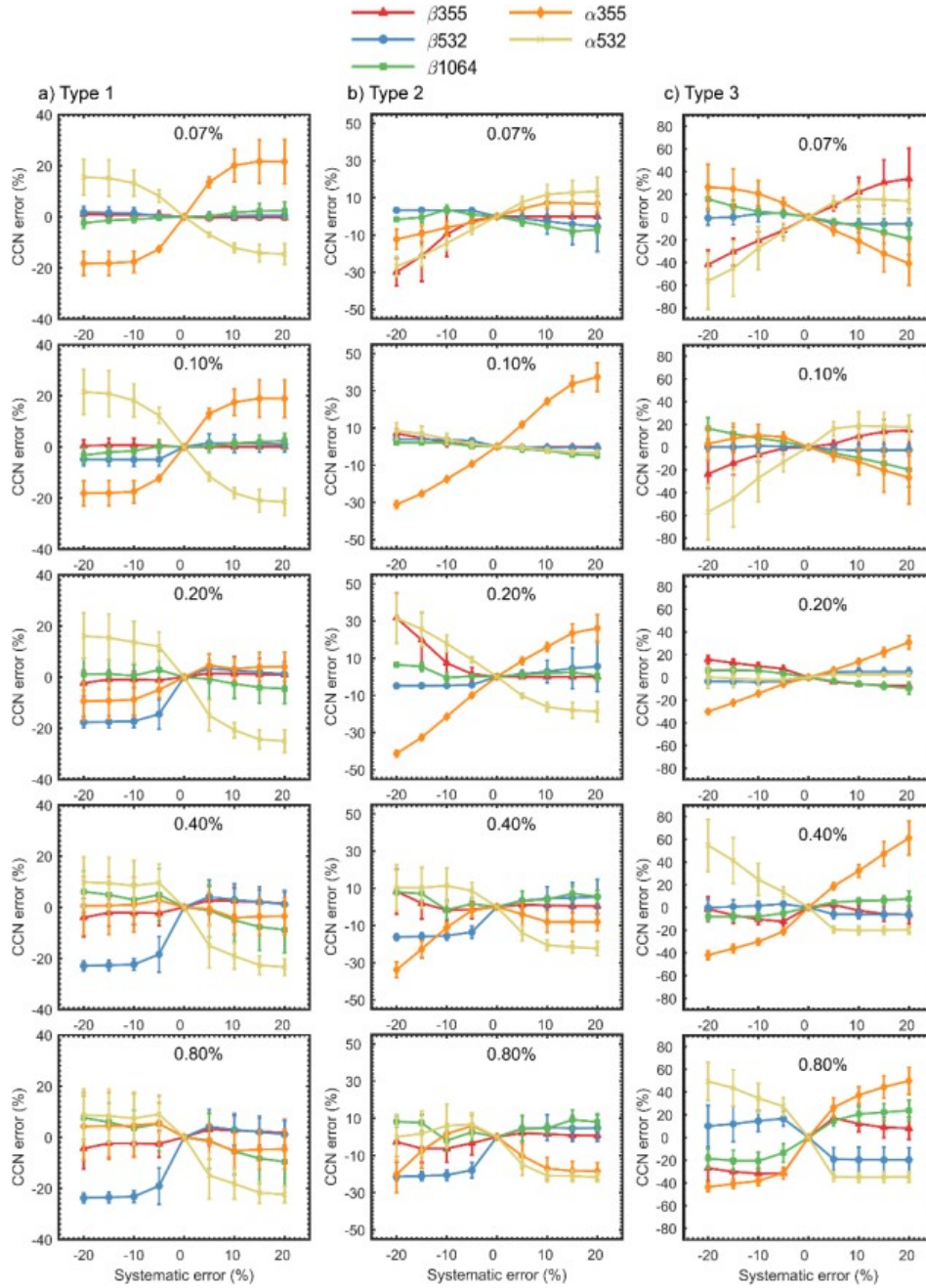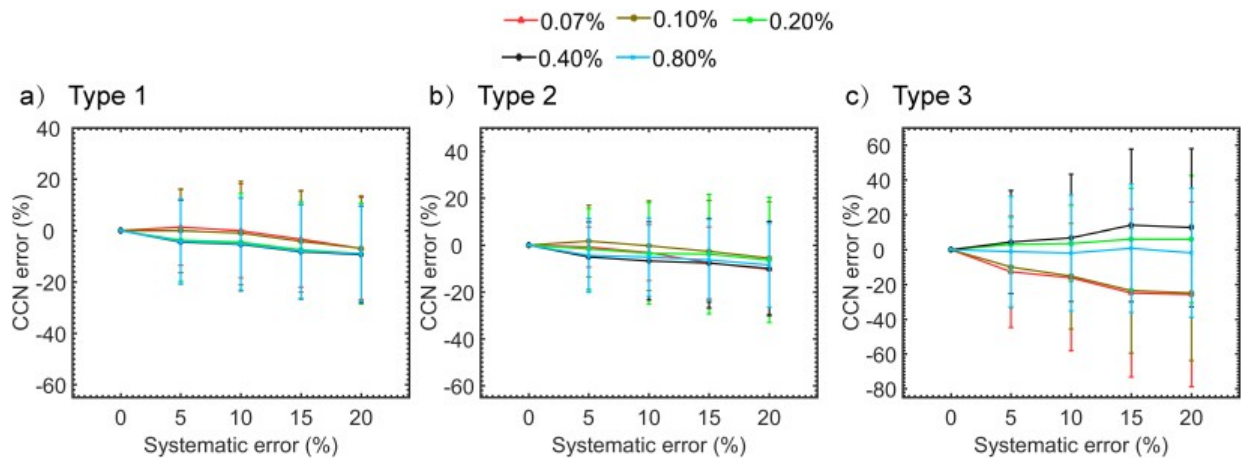
Figure 4. Errors in retrieved CCN number concentrations at different supersaturation ratios (0.07%, 0.10%, 0.20%, 0.40%, and 0.80%) as a function of systematic errors in the input optical data. Error bars denote the standard deviations for (a) Type 1, (b) Type 2, and (c) Type 3 aerosols.
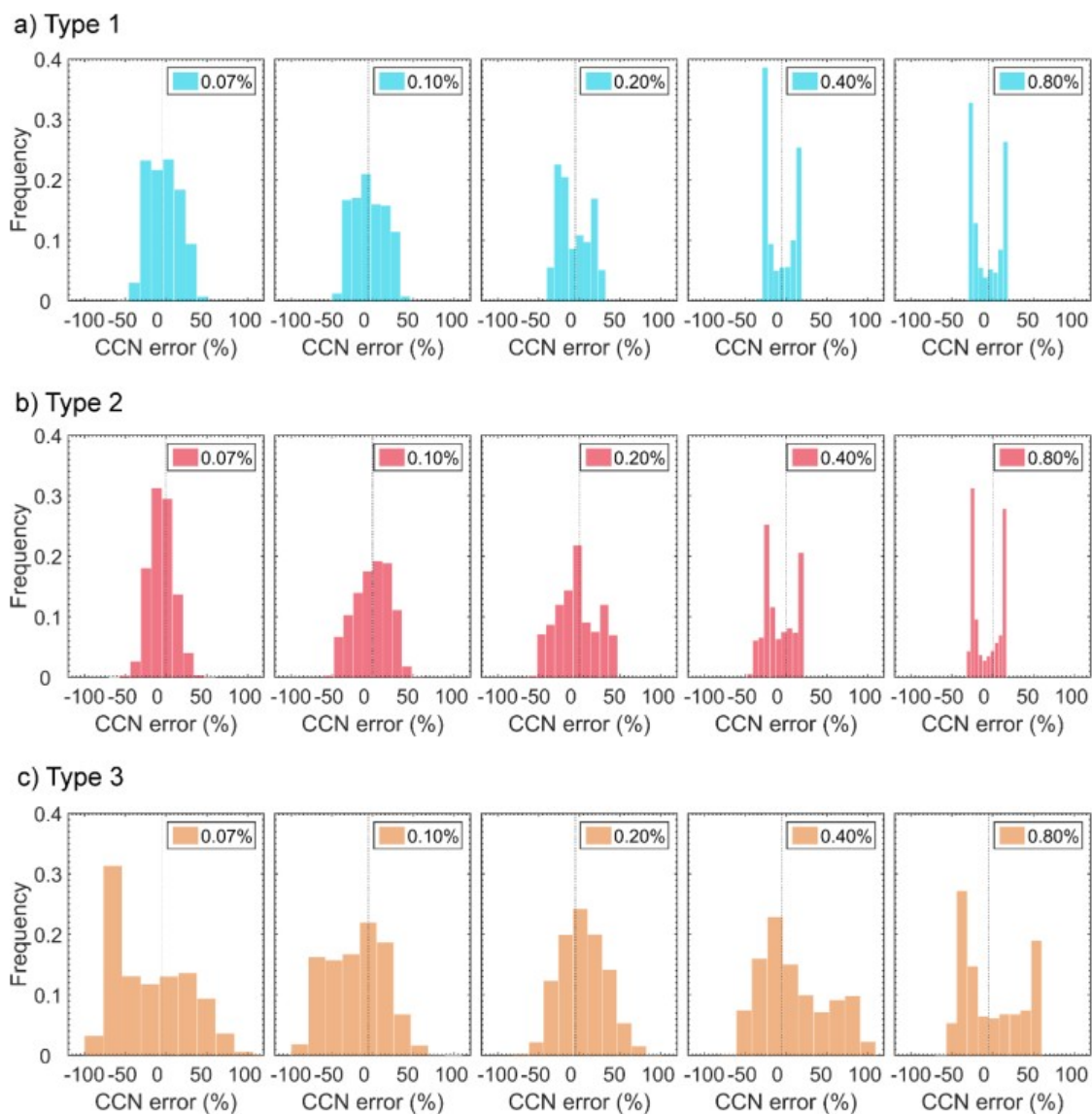
Figure 5. Frequency distributions of CCN errors for (a) Type 1, (b) Type 2, and (c) Type 3 aerosols at different supersaturation ratios (0.07%, 0.10%, 0.20%, 0.40%, and 0.80%) and with 15% random errors for all input optical data.

Figure 6. Errors in retrieved CCN number concentrations at different supersaturation ratios (0.07%, 0.10%, 0.20%, 0.40%, and 0.80%) that arise from accounting for both systematic and random errors for (a) Type 1, (b) Type 2, and (3) Type 3 aerosols. Error bars denote the standard deviations.

816
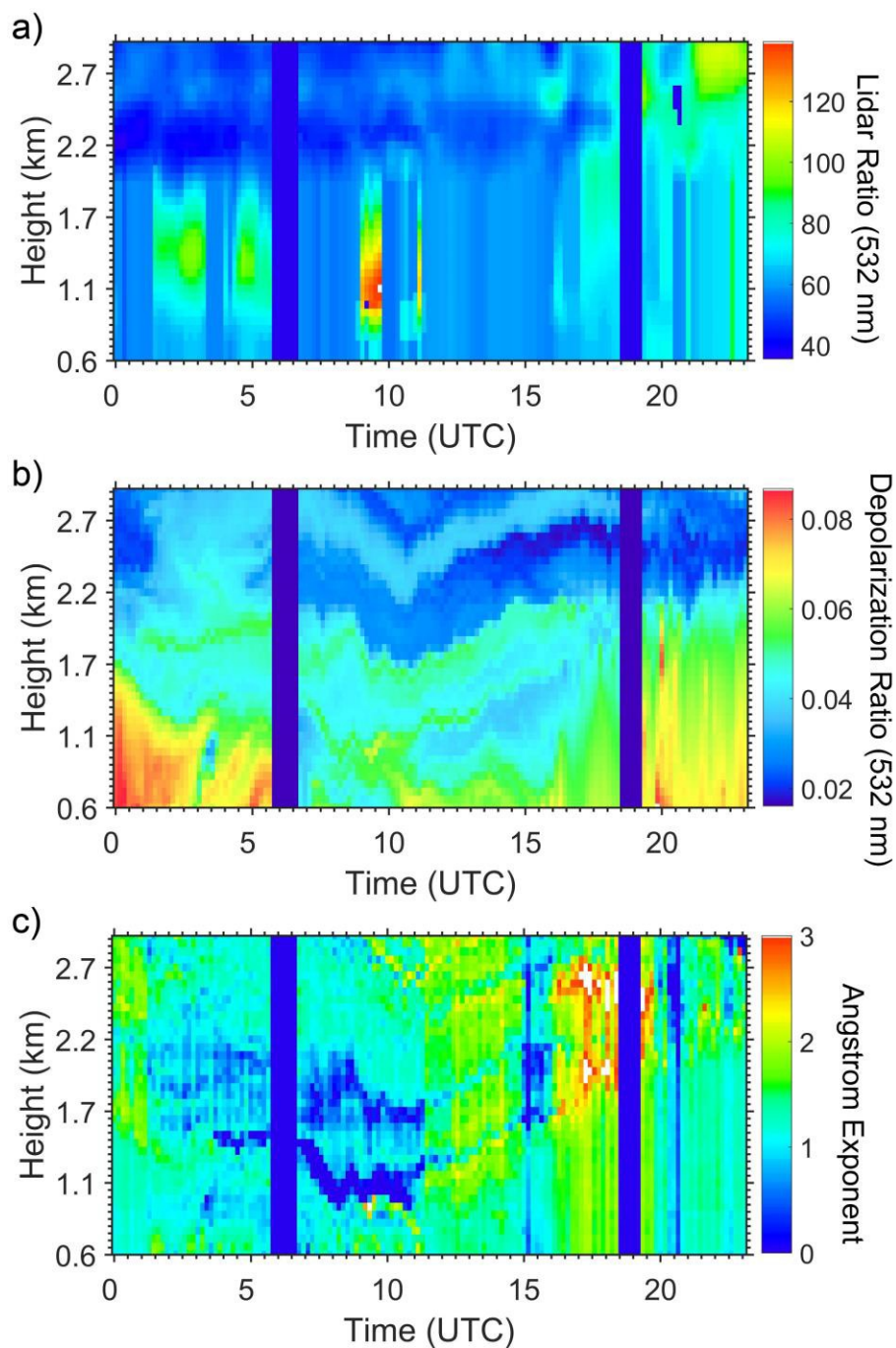
Figure 7. Spatio-temporal distributions of (a) the lidar ratio at 532 nm, and (b) the aerosol depolarization ratio at 532 nm calculated from the Raman nitrogen signal, and (c) the Ångström exponent retrieved from lidar measurements on 16 August 2015 at the SGP site. The heights are kilometers above ground level.
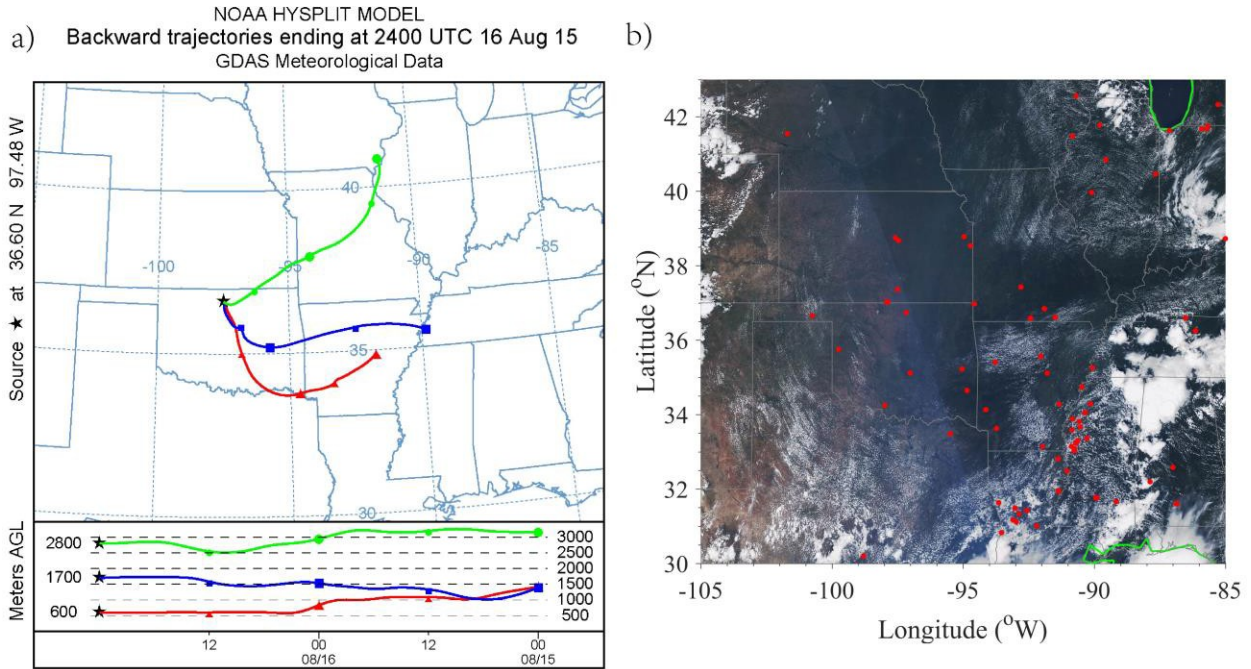
821

822 **Figure 8.** (a) 48-h back trajectories ending at 2400 UTC 16 August 2015 at the SGP site within
823 the 600–2800 m layer, (b) MODIS true RGB image along with fire spots (red dots) from Aqua and
824 Terra on 15 August 2015. The heights are meters above ground level.
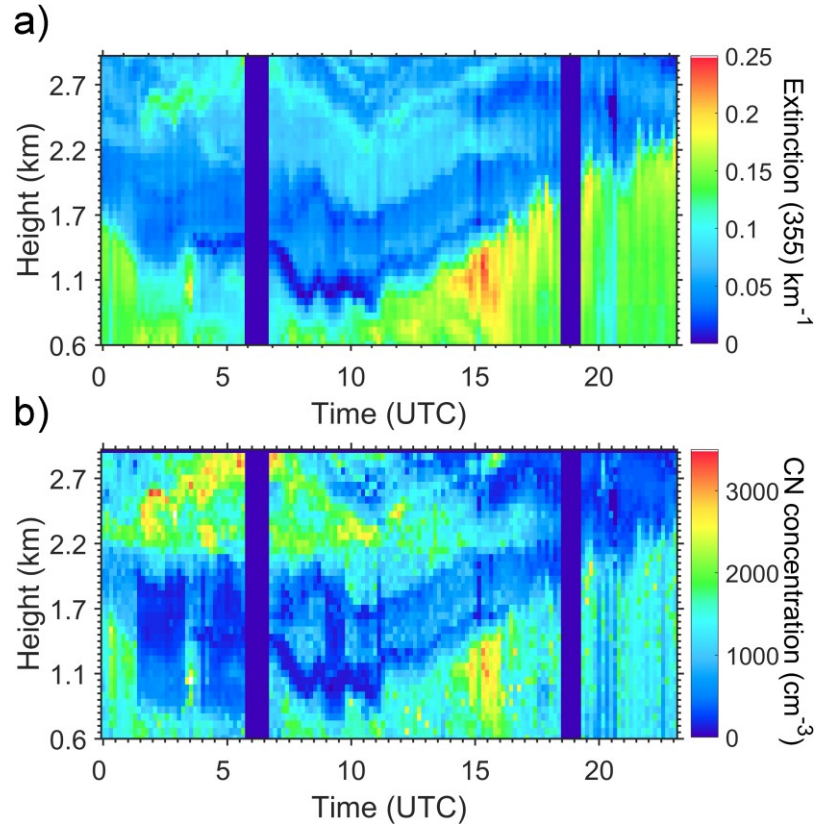
Figure 9. Spatio-temporal distributions of (a) aerosol extinction at 355 nm and (b) CN concentration retrieved from lidar measurements made on 16 August 2015 at the SGP site. The heights are kilometers above ground level.

829
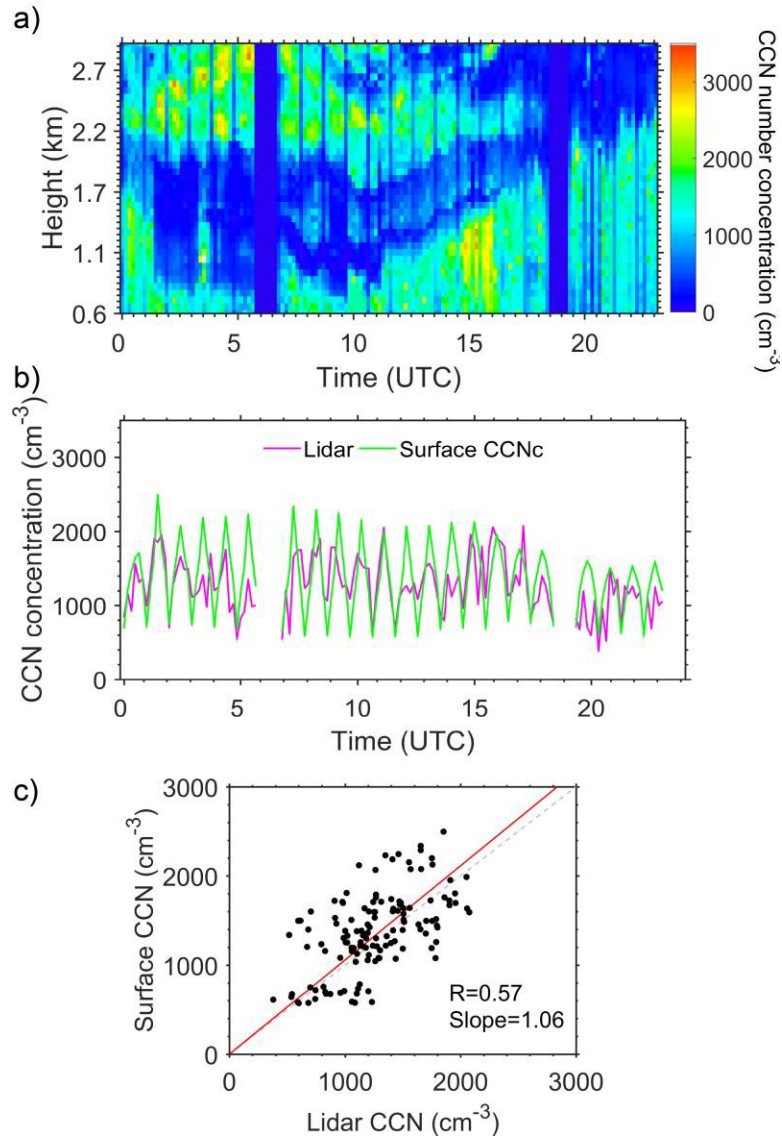
Figure 10. (a) Spatio-temporal distributions of retrieved CCN number concentrations. (b) Time
series of CCN concentration measured by the lidar (at 0.6 km, magenta line) and the surface CCNc
(green line). (c) Surface CCN concentration as a function of lidar CCN concentration (black dots)
on 16 August 2015 at the SGP site. The correlation coefficient (R) and the slope of the linear best-
fit line (red line) are given in the lower right corner of (c). The 1:1 line is also shown (grey dashed
line).

836

Tables

Table 1. Typical parameter ranges for the three aerosol bimodal distributions. V_{tf} / V_{tc} is the ratio of the volume concentration of the fine mode to the coarse mode. m_R and m_I represent the mean values of real and imaginary parts of the complex refractive index [*Dubovik et al.*, 2002; *Veselovskii et al.*, 2004].

Aerosol Parameter	Urban Industrial	Biomass Burning	Dust
$r_f^{\,n}$ (μm)	0.075–0.095	0.072–0.082	0.062–0.082
$r_c^{\,n}$ (μm)	0.60–0.71	0.75–0.80	0.59–0.64
$\ln \sigma_f$	0.38–0.46	0.4–0.47	0.4–0.53
$\ln \sigma_c$	0.70	0.70	0.65
V_{tf} / V_{tc}	0.8–2.0	1.3–2.5	0.1–0.5
m_R, m_I	1.45, 0.01	1.5, 0.015	1.55, 0.002

Table 2. Critical radius at five critical supersaturation ratios for each type of aerosol.

	Critical Radius (r_c, μm)				
	0.07%	0.10%	0.20%	0.40%	0.80%
Type 1 ($\kappa = 0.3$)	0.105	0.083	0.052	0.033	0.021
Type 2 ($\kappa = 0.1$)	0.151	0.119	0.075	0.047	0.029
Type 3 ($\kappa = 0.03$)	0.224	0.177	0.111	0.069	0.043

Table 3. CCN errors at different S_cs (0.07%, 0.10%, 0.20%, 0.40%, and 0.80%) retrieved from error-free inputs for the three aerosol types.

		CCN Error (%)				
		0.07%	0.10%	0.20%	0.40%	0.80%
Mean	Type 1	-0.01 ± 0.24	-0.01 ± 0.24	-0.01 ± 0.24	-0.01 ± 0.24	-0.01 ± 0.24
± SD	Type 2	-0.01 ± 0.18	-0.01 ± 0.18	-0.01 ± 0.18	-0.01 ± 0.18	-0.01 ± 0.18
(%)	Type 3	-0.00 ± 0.21	-0.00 ± 0.25	-0.00 ± 0.27	-0.00 ± 0.28	0.00 ± 0.28

849 **Table 4.** Sensitivity of CCN retrievals to the bimodal fits at different supersaturation ratios (0.07%,
850 0.10%, 0.20%, 0.40%, and 0.80%) from the 50 NAMMA aerosol size distributions. The CCN error
851 is calculated as an absolute value.

	CCN Error (%)				
	0.07%	0.10%	0.20%	0.40%	0.80%
Mean ± SD (%)	3.9 ± 2.8	3.1± 2.9	4.2 ± 3.3	2.2 ± 1.8	1.9 ± 1.6

852

853 **Table 5.** Effects of the assumed $\ln\sigma_c$ on the retrieved CCN errors at different supersaturation ratios
854 (0.07%, 0.10%, 0.20%, 0.40%, and 0.80%) for the three aerosol types. Error-free inputs were used.

		CCN Error (%)				
		0.07%	0.10%	0.20%	0.40%	0.80%
Mean	Type 1	0.01 ± 0.7	-0.03 ± 1.2	-0.03 ± 3.8	0.02 ± 5.2	0.04 ± 5.5
± SD	Type 2	0.8 ± 1.6	0.6 ± 1.0	-0.2 ± 1.2	-1.0 ± 3.0	-1.3 ± 3.9
(%)	Type 3	-0.05 ± 2.7	0. 07 ± 3.3	0.3 ± 1.2	-0.2 ± 2.4	-0.8 ± 5.8

855

856 **Table 6.** Range, mean, and standard deviations of retrieved CCN number concentration errors at
857 different supersaturation ratios (0.07%, 0.10%, 0.20%, 0.40%, and 0.80%). Input optical data
858 included 15% random errors.

		0.07%	0.10%	0.20%	0.40%	0.80%
Type 1	Range (%)	[-53.4, 47.2]	[-49.4, 44.1]	[-37.9, 26.8]	[-30.0, 19.1]	[-27.5, 18.2]
	Mean ± SD (%)	-2.5 ± 18.7	-3.6 ±20.3	-7.0 ± 19.0	-7.6 ± 18.2	-7.3 ± 18.2
Type 2	Range (%)	[-61.7, 50.4]	[-53.0, 51.6]	[-55.1, 44.7]	[-43.8, 21.9]	[-31.2, 16.9]
	Mean ± SD (%)	-5.4 ± 14.6	-1.0 ± 21.4	-3.3 ± 24.9	-7.7± 18.9	-6.5 ± 17.5
Type 3	Range (%)	[-82.7, 122.6]	[-92.0, 103.4]	[-79.4, 98.1]	[-75.4, 103.5]	[-64, 57.7]
	Mean ± SD (%)	-20.0 ± 46.1	-19.4 ± 34.1	4.4 ± 27.5	10.2 ± 41.4	-0.8 ± 36.2

859

860

861

862 **Table 7.** Mean and standard deviations of CCN retrieval errors at different supersaturation ratios

863 (0.07%, 0.10%, 0.20%, 0.40%, and 0.80%) with both systematic and random errors included.

		Systematic error (%)	0.07%	0.10%	0.20%	0.40%	0.80%
Type 1	Mean ± SD (%)	5	1.3 ± 14.7	-0.1 ± 16.3	-3.7 ± 15.9	-4.5 ± 16.3	-4.2 ± 16.6
		10	-0.1 ± 18.3	-0.9 ± 20.2	-4.5 ± 18.9	-5.3 ± 18.1	-5.1 ± 18.0
		15	-3.3 ± 18.7	-4.1 ± 19.7	-7.5 ± 18.8	-8.2 ± 18.3	-8.0 ± 18.4
		20	-6.9 ± 19.9	-6.9 ± 20.5	-8.9 ± 19.6	-9.3 ± 18.8	-9.0 ± 18.7
Type 2	Mean ± SD (%)	5	-0.8 ± 8.5	1.7 ± 15.2	-1.6 ± 17.2	-5.1 ± 14.8	-4.4 ± 15.7
		10	-3.2 ± 11.8	-0.3 ± 19.1	-3.5 ± 21.6	-6.7 ± 16.6	-5.1 ± 16.6
		15	-7.6 ± 15.3	-2.7 ± 21.6	-3.8 ± 25.5	-7.6 ± 19.0	-6.3 ± 17.3
		20	-10.3 ± 19.6	-5.5 ± 24.0	-6.3 ± 26.7	-10.0 ± 20.1	-8.5 ± 17.9
Type 3	Mean ± SD (%)	5	-12.7 ± 32.0	-10.0 ± 23.2	3.0 ± 15.3	4.4 ± 29.5	-1.1 ± 31.7
		10	-16.2 ± 41.9	-15.2 ± 30.4	3.5 ± 21.8	6.8 ± 36.5	-1.9 ± 33.3
		15	-24.9 ± 48.3	-23.5 ± 36.0	6.1 ± 29.2	14.0 ± 43.9	-0.8 ± 36.8
		20	-25.8 ± 53.1	-24.9 ± 38.8	6.0 ± 36.6	12.7 ± 45.4	-1.8 ± 37.0

864